

Bondi-Hoyle-Littleton accretion and the upper mass stellar IMF

Javier Ballesteros-Paredes¹ *, Lee W. Hartmann², Nadia Pérez-Goytia¹,
and Aleksandra Kuznetsova²

¹ *Centro de Radioastronomía y Astrofísica, Universidad Nacional Autónoma de México, Apdo. Postal 72-3 (Xangari), Morelia, Michoacán 58089, México*

² *Department of Astronomy, University of Michigan, 500 Church Street, Ann Arbor, MI 48105, USA*

Submitted to MNRAS, 2 March 2024

ABSTRACT

We report on a series of numerical simulations of gas clouds with self-gravity forming sink particles, adopting an isothermal equation of state to isolate the effects of gravity from thermal physics on the resulting sink mass distributions. Simulations starting with supersonic velocity fluctuations develop sink mass functions with a high-mass power-law tail $dN/d\log M \propto M^\Gamma$, $\Gamma = -1 \pm 0.1$, independent of the initial Mach number of the velocity field. Similar results but with weaker statistical significance hold for a simulation starting with initial density fluctuations. This mass function power-law dependence agrees with the asymptotic limit found by Zinnecker assuming Bondi-Hoyle-Littleton (BHL) accretion, even though the mass accretion rates of individual sinks show significant departures from the predicted $\dot{M} \propto M^2$ behavior. While BHL accretion is not strictly applicable due to the complexity of the environment, we argue that the final mass functions are the result of a *relative* M^2 dependence resulting from gravitationally-focused accretion. Our simulations may show the power-law mass function particularly clearly compared with others because our adoption of an isothermal equation of state limits the effects of thermal physics in producing a broad initial fragmentation spectrum; $\Gamma \rightarrow -1$ is an asymptotic limit found only when sink masses grow well beyond their initial values. While we have purposely eliminated many additional physical processes (radiative transfer, feedback) which can affect the stellar mass function, our results emphasize the importance of gravitational focusing for massive star formation.

Key words: stars: formation — stars: luminosity function, mass function — ISM: clouds

1 INTRODUCTION

The origin of the stellar initial mass function (IMF) has been the subject of many theoretical studies over the years, with little resulting consensus. As discussed in the recent review by Offner et al. (2013), currently popular theories may be classified into two groups: one in which masses of dense structures or cores created as a result of (supersonic) turbulence map into the resulting stellar masses (e.g., Padoan & Nordlund 2002; Hennebelle & Chabrier 2008, 2009), while the other invokes accretion from an extended region with dynamical interactions between self-gravitating gas and stars (e.g., Bonnell et al. 2001a,b; Bate et al. 2003;

Clark et al. 2007). Although there seems to be general agreement that thermal physics plays an essential role in the turnover of the IMF in the solar-mass (and below) regime (Jappsen et al. 2005; Bonnell et al. 2006; Bate 2012; Krumholz et al. 2010; Myers et al. 2014), the application of Jeans mass-type arguments is far less clear for massive stars, where continuing accretion from regions beyond the local Jeans lengths is plausible (Bonnell et al. 2001a).

One plausible explanation for the upper mass IMF is gravitationally-focused mass addition, sometimes referred to as “Bondi-Hoyle” (Zinnecker 1982; Bonnell et al. 2001a,b) or “Bondi-Hoyle-Littleton” accretion (BHL; Edgar 2004), with an accretion rate given by

* e-mail: j.ballesteros@crya.unam.mx

$$\dot{M} = \frac{4\pi G^2 M^2 \rho_\infty}{(c_s^2 + v^2)^{3/2}} \equiv \alpha M^2, \quad (1)$$

where \dot{M} is the mass accretion rate, M is the gravitating central mass, and ρ_∞ , c_s , and v_∞ are the ambient gas density, the (isothermal) sound speed, and the relative velocity of the ambient gas, respectively. Zinnecker (1982) showed analytically that, if α is constant, a population with a small but finite difference in initial masses will evolve to an asymptotic power law slope of $\Gamma = d \log N / d \log M = -1$. This is a suggestive result, given the apparent universality (within observational uncertainties) of the Salpeter slope $\Gamma_s \sim -1.35$ for high-mass stars (Bastian et al. 2010), and recognizing that the $\Gamma \rightarrow -1$ is an asymptotic limit reached only when the accreted masses far exceed initial values (Zinnecker 1982).

However, the applicability of BHL accretion in massive star formation has been challenged recently by Maschberger et al. (2014, M14); (see also Padoan et al. 2014). M14 analyzed the results of formation of sink particles in a hydrodynamic simulation and argued that the accretion rates are generally $\dot{M} \propto M^{2/3}$, a result predicted for the case of accretion in a gas-dominated potential (Bonnell et al. 2001a,b) rather than the rate of equation (1), which applies to accretion in a “stellar-dominated potential” (Bonnell et al. 2001a,b). M14 found that the sink accretion follows “non-linear stochastic processes”, and concluded that the upper IMF power-law is not a result of BHL accretion.

One of the problems in analyzing the results of numerical simulations in terms of equation (1) is that α is not constant, because the medium surrounding accreting objects is highly structured and time-variable. In addition, it is not trivial to relate the relative velocity in equation (1), which is presumed to be that of the “ambient medium” far from the (isolated) accreting mass, with the motions observed in simulations with many gravitating regions, including both sinks and gas (see, e.g. Bonnell et al. 2001a). Nevertheless, if equation (1) is interpreted as referring to an average over volume and time, it may still be relevant for the formation of massive objects, as gravitational acceleration must be present, especially on large scales.

As numerical simulations of the stellar IMF become increasingly sophisticated, with ever-more complex physics (e.g., complex equations of state, radiative transfer, stellar feedback), it becomes increasingly difficult to isolate the effects of individual assumptions. These considerations motivated us to take a simplified approach. In this paper, we present numerical experiments intended to address the effects of gravity on the development of upper-mass power-law IMFs. We assume isothermality, which allows us to minimize the importance of (and uncertainties in) thermal physics, and easily produce sufficient numbers of gravitationally-bound systems (sink particles) to provide reasonable statistics for the upper-mass IMF slope Γ .

Our simulations starting with supersonic but decaying turbulence produce an upper-mass sink mass function with $\Gamma = -1 \pm 0.1$; the run starting with density fluctuations produced a power-law upper mass tail of comparable slope which emerges at later times. Thus, we find the power-law behavior predicted by Zinnecker (1982), even though a simplistic application of equation (1) with $\alpha = \text{constant}$, does not reproduce the evolving nature of the simulations. We

argue however that these departures from the simple model can be reconciled with the simulations by taking into account the *local* depletion of matter in the environments of the sinks and the mass dependence of the time of sink formation. While our calculations are of a highly simplified situation compared with that of real star-forming regions, they nevertheless demonstrate the potential of gravitational focusing to explain the upper mass power law of the IMF.

2 METHODS

2.1 Numerical simulations and initial conditions

We performed numerical simulations of isothermal gas to represent the interior of a small (\sim parsec size) molecular cloud. We used the N -body, smoothed particle hydrodynamics (SPH) code Gadget 2 (Springel 2005) with the inclusion of sink particles as in Jappsen et al. (2005). Sink particles thus represent stars in the sense that they do not have gas properties any more, and that the mass that fell into them will not emerge back into the medium. Since we do not include radiative feedback or stellar heating, their interaction with the gas was via gravitational forces only.

Our simulations were performed using 6 million particles, with a total mass of $1000 M_\odot$, in a cubic box of side 1 pc in all simulations but one, which was performed in a box 3 pc on a side. Sink creation was allowed above densities of $1.7 \times 10^7 \text{ cm}^{-3}$, with an outer radius of $R_{\text{out}} = 1.8 \times 10^{-3}$ pc within which no further sinks may be made, and an inner sink radius of $R_{\text{in}} = 1.8 \times 10^{-4}$ pc or 37 AU. All runs were isothermal with an adopted $T = 10$ K. According to the Bate & Burkert (1997) criterion, our mass resolution limit is $\sim 0.013 M_\odot$; in practice nearly all of the sink initial masses were $\gtrsim 0.03 M_\odot$. Gas is accreted into sinks if the particles are within R_{out} and are gravitationally-bound to the sink, checking previously that another sink does not preferentially accrete the particle, or if the gas particle passes within R_{in} . As our sink particles exert gravity, we impose a gravitational smoothing length of 0.003 pc.

Table 1 shows the main parameters of our runs. Note that because these simulations are isothermal, they can be rescaled (see Hsu et al. 2010). We imposed initial velocity fluctuations with a pure rotational velocity power spectrum with random phases and amplitudes (e.g., Stone et al. 1998), and with a peak at wavenumber $k_{\text{for}} = 4\pi/L_0$, where L_0 is the linear size of the box. No forcing at later times is imposed. All calculations but run 33 were evolved for ~ 1.1 free-fall times defined by the initial density in the computational box (see Table 1).

In the case of run 33, the velocity field was set to zero, and initial density fluctuations $\delta\rho$ were imposed, following a Kolmogorov $P_k \propto k^{-11/3}$ spectrum with positive amplitudes only. We then stretched these fluctuations such that the density field was set to

$$\rho = 10^{(\log \delta\rho - \langle \log \delta\rho \rangle)^{1.5}} \quad (2)$$

Snapshots of the properties of the simulations were taken every 10^4 yr, except in the cases of runs 22HR and 32 for which snapshots were produced every 1000 and 5000 yr, respectively.

We note that all of the runs in Table 1 were actually

Table 1. Parameters of the simulations

Name	Mach #	Mass (M_\odot)	Size (pc)	n_0 (cm^{-3})	M_J (M_\odot)	τ_{ff} (Myr)	$\tau_{\text{end}}/\tau_{\text{ff}}$	Δt_{dump} (yr)
22	8	1000	1	17,000	0.48	0.24	1.17	1×10^4
22HR	8	1000	1	17,000	0.48	0.24	1.08	1×10^3
23	16	1000	1	17,000	0.48	0.24	1.00	1×10^4
24	4	1000	1	17,000	0.48	0.24	1.17	1×10^4
32	8	1000	3	630	2.5	1.26	1.19	5×10^3
33	0	1000	1	17,000	0.48	0.24	0.75	1×10^4

performed twice, with the same parameters but with different initial random seeds. In the following discussion the figures generally show the results of one of the two calculations, except for the mass functions where we add the results of both sub-runs to improve the statistics on the slope of the mass function.

2.2 Measuring local properties around the sinks

Following eq. (1), we will need to calculate the density ρ_0 and velocity dispersion v_{turb} of the gas around each sink. To do so, it is necessary to define some arbitrary radius. In principle, it is desirable to calculate these properties outside the Bondy-Hoyle radius, given by

$$R_{BH} \equiv 2GM/v_{\text{tot}}^2 = 8.6 \times 10^{-3} \text{ pc } (M/M_\odot)(v_{\text{tot}}/\text{km sec}^{-1})^{-2}, \quad (3)$$

(with $v_{\text{tot}}^2 = (v_{\text{turb}}^2 + c_s^2)$ [see eq. (1), v_{turb}^2 is the turbulent, or non-thermal velocity dispersion of the gas around the star, and c_s is the sound speed]). As can be seen, while the velocity dispersion defines the BH radius, it in turn depends on the size of the volume at which the measurement is taken. Furthermore, since statistically speaking, the velocity dispersion increases with size, the larger the volume, the larger the velocity dispersion and the smaller the Bondi-Hoyle radius. To measure v_{turb} , we have, thus, taken a compromise: a volume large enough to ensure to take measurements at least at 3 times the BH radius, but small enough to not get a BH radius that is arbitrarily small. Thus, we have calculated the velocity dispersion and the mean density of the sph particles that are within $l = 6$ times the outer radius for accretion, **Router**, and verified that $R_{BH} \leq 3 \times \text{Router}$ in all cases.

3 RESULTS

3.1 Initial velocity perturbations

Figure 1 shows a projection of the evolution of the density integrated through the computational box, along with sink particles as they form, at four times for run 22. The initial supersonic velocity fluctuations shock and rapidly dissipate energy, resulting in a (typical) complex distribution of dense clumps and filaments. The gas then globally collapses under its own self-gravity, the density in the clumps and filaments increase, ultimately forming sink particles which then continue to accrete from the environment.

We calculated accretion rates into sinks \dot{M} as the difference in sink mass between two snapshots, as a function

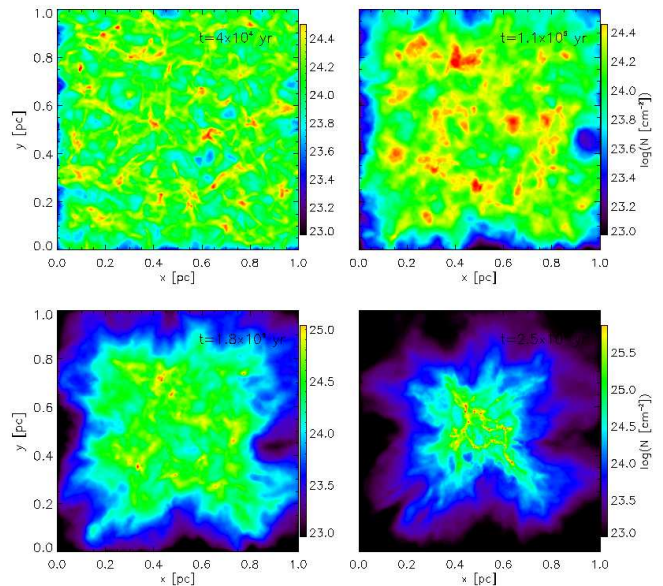


Figure 1. Column density of run 22 at times 0.4, 1.1, 1.8 and 2.5×10^5 yr.

of mass. In Figure 2 we show the time sequence of accretion rates of sinks as a function of mass ($M(\text{sink})$). While the dependence of the accretion rates on sink mass is crudely comparable to the $\dot{M} \propto M^2$ prediction of the simple model, there are departures. At the low-mass end of the mass function ($M(\text{sink}) \sim 0.1M_\odot$), there is a large spread in the accretion rate at a given mass, while at the high mass end, the spread in accretion rate *vs.* mass is much less, but the slope is flatter than M^{-2} , with an approximate $M^{1.5}$ dependence at the end of the simulation for the high-mass sinks. These departures from the prediction of equation (1) are due to the reduction of matter in the environments of the sinks as mass is accreted, and the time dependence of sink creation as a function of mass (see discussion in §4). The low-mass sinks are particularly affected by “competitive accretion” (e.g., Bonnell et al. 2001a,b), where mass is gravitationally attracted to other sinks, particularly the higher-mass ones. This competition results in more low-mass sinks exhibiting very low accretion rates at later times.

Figure 3 shows the evolution of the sink mass function as a function of time for run 22 (a summation of two individual runs with different random seed initializations for the phases and amplitudes of the velocity fluctuations). In-

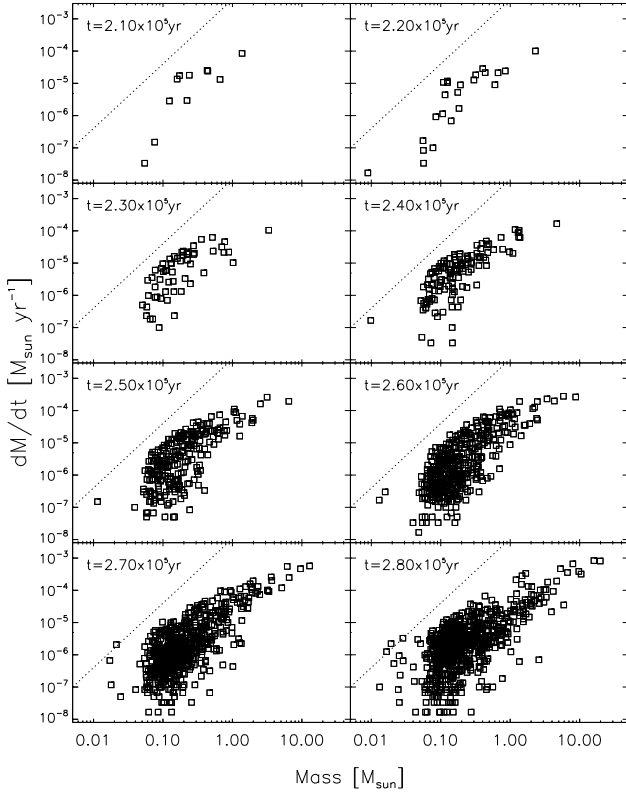


Figure 2. Accretion rates into the sinks \dot{M} vs. the mass of the sinks $M(\text{sink})$ for run 22 from $t = 2.1$ to 2.8×10^5 yr. The dotted line indicates a slope $dM/dt \propto M(\text{sink})^2$.

terestingly, a quasi-power law distribution of masses is established quite early. Most of the sinks are formed at low masses $\sim 0.05 - 0.1 M_\odot$. The slope of the power-law is roughly $\Gamma \sim -1$ over most of the period of sink formation, but it is not until the end of the calculation that the statistics become good enough to calculate it accurately. Measuring from a low mass of $0.2 M_\odot$ to the upper limit yields $\Gamma = -1.12 \pm 0.07$ or from $0.5 M_\odot$, $\Gamma = -1.15 \pm 0.10$.

In Figure 4 we show the final IMFs for the four runs 23, 24, and 32. are $\Gamma = -1.24 \pm 0.30$, -1.04 ± 0.07 , and -0.96 ± 0.10 for runs 23, 24, and 32, respectively, measuring from the $0.5 M_\odot$ bin, with essentially the same results measuring from $0.2 M_\odot$. The first three runs demonstrate that changing the Mach number of the initial velocity fluctuations makes essentially no difference to the final results. Run 32 consists of the same mass within a volume 27 times larger and thus an initial density that factor smaller; the resulting IMF is identical within errors to the others. This demonstrates the scale-free nature of the problem, with the peak in the mass function controlled by the basic resolution of these isothermal simulations. Note that we achieve a $\Gamma \sim -1$ power-law mass function despite the departures of the accretion rates from a strict $\dot{M} \propto M(\text{sink})^2$ relation (§4.1).

In Figure 5 we use run 32 to explore the onset of the sink mass function in more detail. As the initial free-fall time of this simulation is a factor of 5.2 longer than in the other

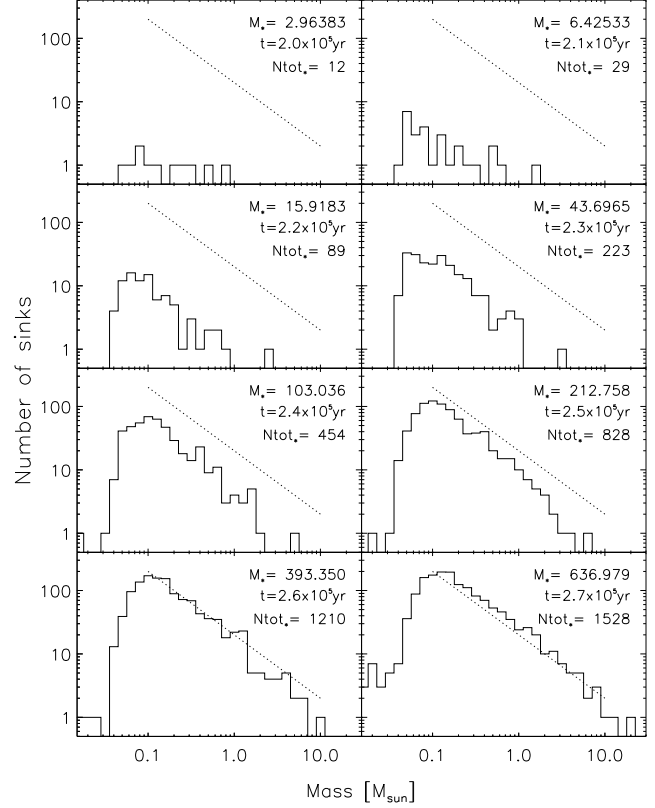


Figure 3. The IMFs for run 22, summed over the two random initializations, from $t = 2.0$ to 2.7×10^5 yr (compare with Figure 2). The dotted line indicates a power law slope $\Gamma = -1$.

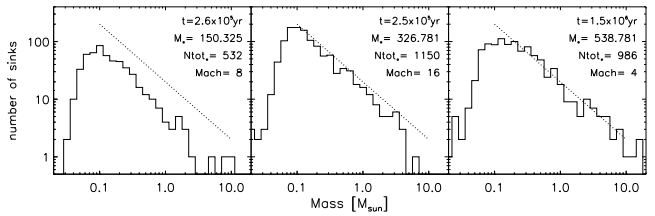


Figure 4. The final IMFs for individual runs 23, 24, and 32.

runs, and snapshots were dumped every 5000 yr, this simulation effectively provides higher time resolution (recall that the isothermal nature of the simulations permits straightforward rescaling). With higher (effective) time resolution, the early development of a quasi-power law distribution of sink masses is observed clearly.

3.2 Initial density fluctuations

Figure 6 shows the surface density for run 33 at $t = 0.4, 1.1, 1.8$ and 2.5×10^5 yr. The adopted initial conditions are such that the density fluctuations are mostly confined to a few large-scale concentrations at early times. The ensuing gravitational collapse results in the formation of much larger-scale filaments, with much more linear collections of

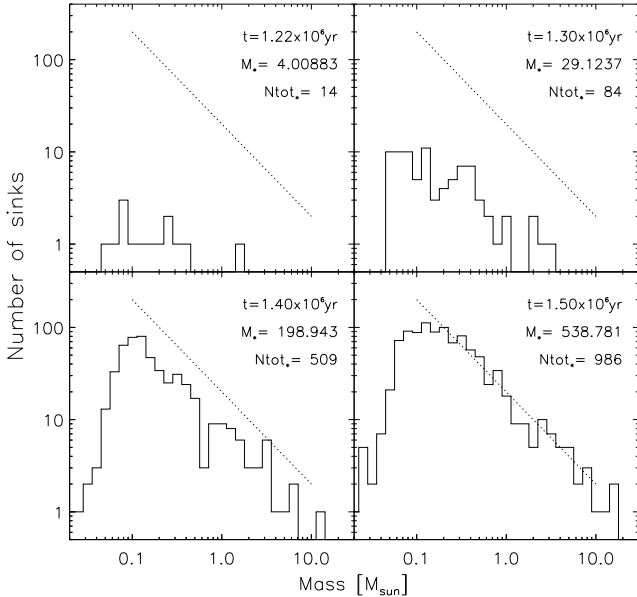


Figure 5. IMFs for run 32 at $t = 1.22, 1.3, 1.4$ and 1.5×10^6 .

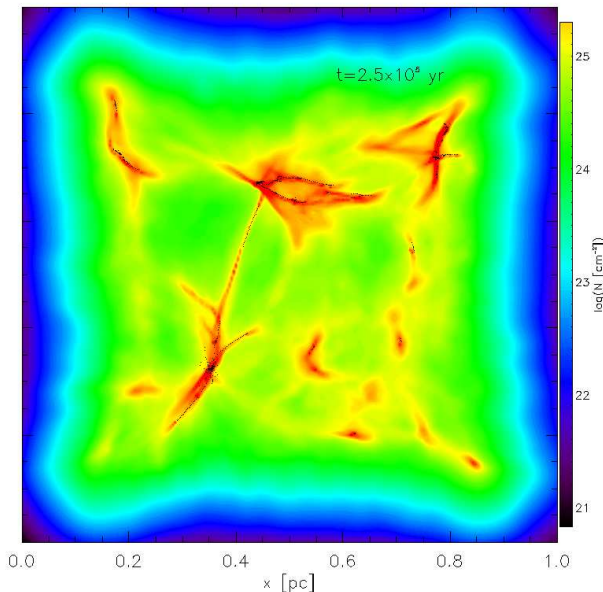


Figure 6. Column density at $t = 2.5 \times 10^5$ yr for run 33. Black dots denote the current positions of the sinks.

sink particles than in the velocity fluctuation cases (Figure 1).

In Figure 7 we show \dot{M} vs. $M(\text{sink})$ at various times. The accretion rates show considerably less correlation with sink mass than for the velocity fluctuation case (Figure 2). This difference is probably due to the differing spatial distributions of the sinks, especially at early times. In the density fluctuation case, the dense regions initially are far more spatially concentrated into narrow filaments, resulting in higher concentration of sinks and thus more competition for acc-

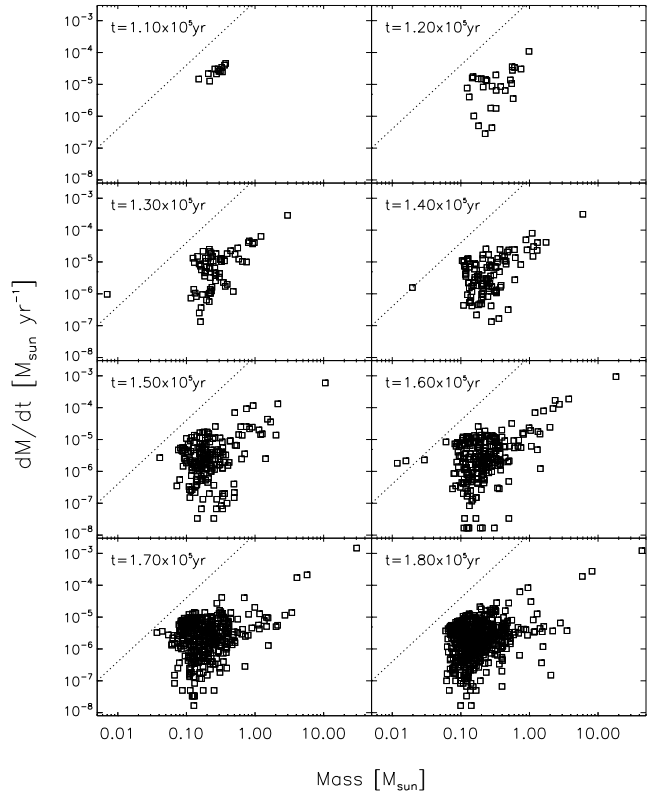


Figure 7. \dot{M} vs. $M(\text{sink})$ for run 33 from $t = 1.1$ to 1.8×10^5 yr.

retable mass, causing more scatter in accretion rates at a given mass (compare Figure 6 to Figure 1).

Figure 8 shows the development of the sink mass function for run 33. The evolution differs from that of the velocity fluctuation cases in that a quasi-log-normal distribution emerges initially, consistent with the weaker correlation of accretion rates with mass. However, even in this case, a roughly power-law tail develops at later times, with an evolution arguably toward $\Gamma \sim -1$, although the statistics are not good enough to make an accurate slope measurement.

4 DISCUSSION

4.1 Is BHL accretion relevant?

The standard BHL accretion equation (1) does not apply directly to our simulations because it envisages a well-defined external medium from which to accrete which is unperturbed by any gravitational field other than that of the central mass. This is manifestly not the case because the self-gravity of the gas is important and even dominant early on, and many other gravitating objects are present. Nevertheless, the development of the power-law mass function with $\Gamma = -1$ as predicted suggests that some basic feature of BHL accretion dominates the production of the mass function even in the more complex situation.

In the simple BHL model, using equation (1) and as-

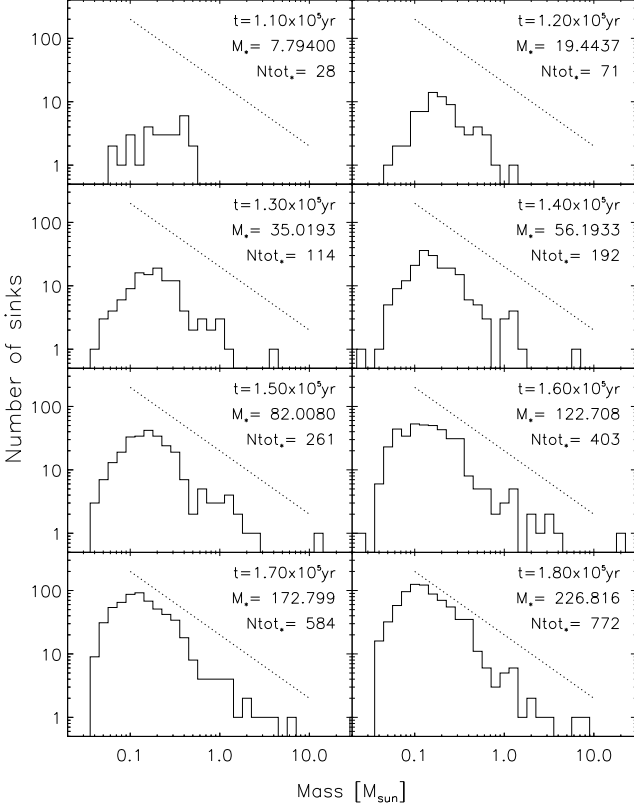


Figure 8. IMFs for density-fluctuation run 33 from $t = 1.1$ to 1.8×10^5 yr.

suming $\alpha = \text{constant}$, the growth of the accreting mass as a function of time is

$$M = \frac{M_0}{1 - \alpha M_0 t}, \quad (4)$$

where M_0 is the mass at $t = 0$. From this, Zinnecker (1982) showed that the resulting mass function $\zeta = dN/d \log M$ for an initial population of masses $M_{0,i}$ with a mass distribution $\zeta_0 = \zeta(t = 0)$ is of the form

$$\zeta(M) = \zeta_0 \left(\frac{M}{1 + \alpha M t} \right) (1 + \alpha M t)^{-1}. \quad (5)$$

More generally, recognizing the environment of the sinks is both temporally and spatially variable, one may write the accretion rate as

$$\dot{M} = \alpha(t, \mathbf{r}) M^n. \quad (6)$$

Even if α is not constant, if it does not depend on M either explicitly or implicitly, the analysis of the Boltzmann continuity equation made by Zinnecker (1982) is applicable, and the asymptotic mass function $\zeta = dN/d \log M$ has the form

$$\zeta(M) \propto \frac{d \log M_0}{d \log M_f} \propto M^{-(n-1)}, (n > 1). \quad (7)$$

While the mass function slope $\Gamma = -1.0 \pm 0.1$ that we observe in our velocity-fluctuation simulations indicates $n = 2$, the snapshots themselves naively suggest accretion rates for the most massive sinks with a shallower mass dependence $n \sim 1.5$ (e.g., Figure 2) which would imply $\Gamma \sim -0.5$.

It is important to recognize that the mass accretion rates of the sinks, integrated over time, *must* map into the mass function. To resolve this apparent contradiction, we notice, first of all, that sinks are typically formed in groups: in Fig. 9 we show a snapshot of run 22ID2 (upper panel) and 32 (lower panel) at relatively early times, i.e., when only 64 and 50 sinks have been formed, respectively ($t = 220,000$ yr, equivalent to 0.91 free-fall times (t_{ff}) for run 22ID2, and 1.325 Myr, equivalent to $1.05 t_{ff}$ for run 32). Thus, at first glance it could be arguable that such groups share similar environmental properties (density and velocity dispersion).

We also note that, since $\alpha = \alpha(t, \mathbf{r})$, local variations in α may blur any quadratic dependence of \dot{M} on M at a given time. Thus, by dividing the mass accretion rate of each sink by its local α , it might be possible to recover any power-law dependence (eq. [6]) of the accretion mass rate with mass, at least by groups with similar environmental properties (i.e., similar α):

$$\log \dot{M} = \log \alpha_i(t, \mathbf{r}) + n \log M, \quad (8)$$

In Fig. 10 we now plot the ratio¹ \dot{M}/α' against the mass M for all the sinks at the same times shown in Fig. 9. In both cases we notice that there are two main groups, each one sharing the approximate tendency $\dot{M} \propto M^2$, but with an offset of ~ 3 orders of magnitude between them. This result shows that different groups of sinks might have different environmental properties, and thus, any possible relationship of the kind $\dot{M} \propto M^2$ might be blurred when the groups are analyzed all together.

To worsen the case, we furthermore notice that even when one can account for such kind of segregation by α_i , the situation might still not be straightforward. For instance, in the upper panel of Fig. 10 (which corresponds to run 22ID2) we denote by empty squares all the sinks at $t = 1.03 t_{ff}$ but those that belong to the group that it is zoomed in in the upper panel of Fig. 9. The 16 sinks that belong to that group are denoted also with cyan asterisks if the value of α' is smaller than 10^{-13} , and by red crosses otherwise. We then notice in the upper panel of Fig. 10, that all but one sinks that belong to the mentioned group have $\alpha' < 10^{13}$, and that only one of them (red symbol) has $\dot{M}/\alpha' > 10^{-13}$. This sink is also denoted by a cross in the zoom of the upper panel of Fig. 9 (the remaining ones are denoted by asterisks), and even though it is the neighborhood of the group, in the upper panel of Fig. 10 it falls far away from the $\dot{M}/\alpha' \propto M^2$ tendency delineated by the rest of the group. The reason might be either that the local density of this sink is smaller than that of the rest of the group (e.g., it is located in the periphery of the core), or that somehow this sink has a larger velocity (e.g., the sink its been ejected), compared to the rest of the group, increasing the velocity dispersion of the sph particles of its neighborhood. In fact, a careful analysis of the zoom in the upper panel of Fig. 9 shows that it might be the first case: the sink is located in the periphery of the core, according to the column density map.

In a similar way, we notice that each one of the four groups of sinks shown in the lower panel of Fig. 9, also exhibit the approximate $\dot{M} \propto M^2$ tendency, although with some scatter, (see lower panel of Fig. 10), and even with

¹ In what follows, since $\alpha \propto \rho/v_{tot}^3$ we will define $\alpha' \equiv \rho/v_{tot}^3$

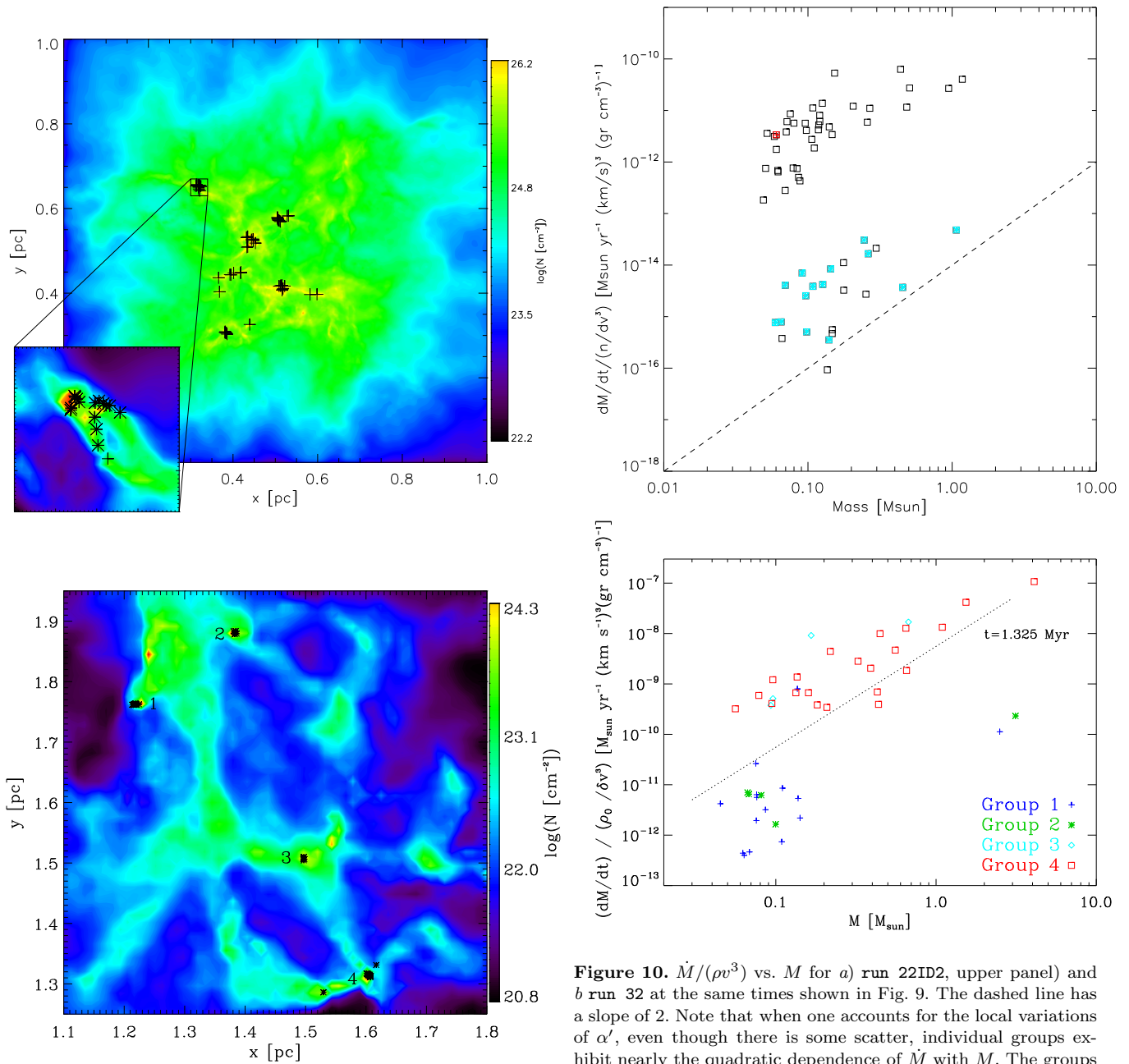


Figure 9. Maps of runs 22ID2 (a, upper panel) and 32 (b, lower panel) at $t = 220,000$ yr and at 1.325 Myr, respectively. In both cases sinks are formed by groups, where apparently, the local density and velocity dispersion of the gas is nearly the same for all the sinks in the group. Closer examination shows that this is not necessarily the case (see text).

some outliers (e.g., blue cross in group 1 showing $\dot{M}/\alpha' \sim 5 - 8 \times 10^{-10}$). These results suggest that even within a single group, there might be different values of v_{tot} and ρ , and then, strong scatter in the plane ($M, \dot{M}/\alpha'$) might be seen.

To further stress this point, in Fig. 11 we plot again \dot{M}/α' vs. M for the same two runs, but (a) at later times, when substantially more sinks have been formed (363 for run 22ID2, upper panel, and 354 for run 32, lower panel), and

Figure 10. $\dot{M}/(\rho v^3)$ vs. M for a) run 22ID2, upper panel) and b) run 32 at the same times shown in Fig. 9. The dashed line has a slope of 2. Note that when one accounts for the local variations of α' , even though there is some scatter, individual groups exhibit nearly the quadratic dependence of \dot{M} with M . The groups labeled in the lower panel are the same than those shown in the lower panel of Fig. 9.

then the density and velocity fields are even more complex, and (b) in both cases, we color and label every point according to the local value of α' (the actual values are colored and labeled in log scale in the inner box). Although there is some scatter at every α' , it is clear that in each case we recover the quadratic dependency per groups, strongly suggesting that, indeed, the accretion is of Bondi-Hoyle type, with non-constant α , as would be predicted by eq. (8) for $n = 2$ and different α . In summary, *even for a single group, substantial scatter in the plane ($M, \dot{M}/\alpha'$) can be due to local fluctuations in velocity or density. These fluctuations blur the quadratic dependence of \dot{M}/α' with M .*

Since individual groups show the quadratic dependence

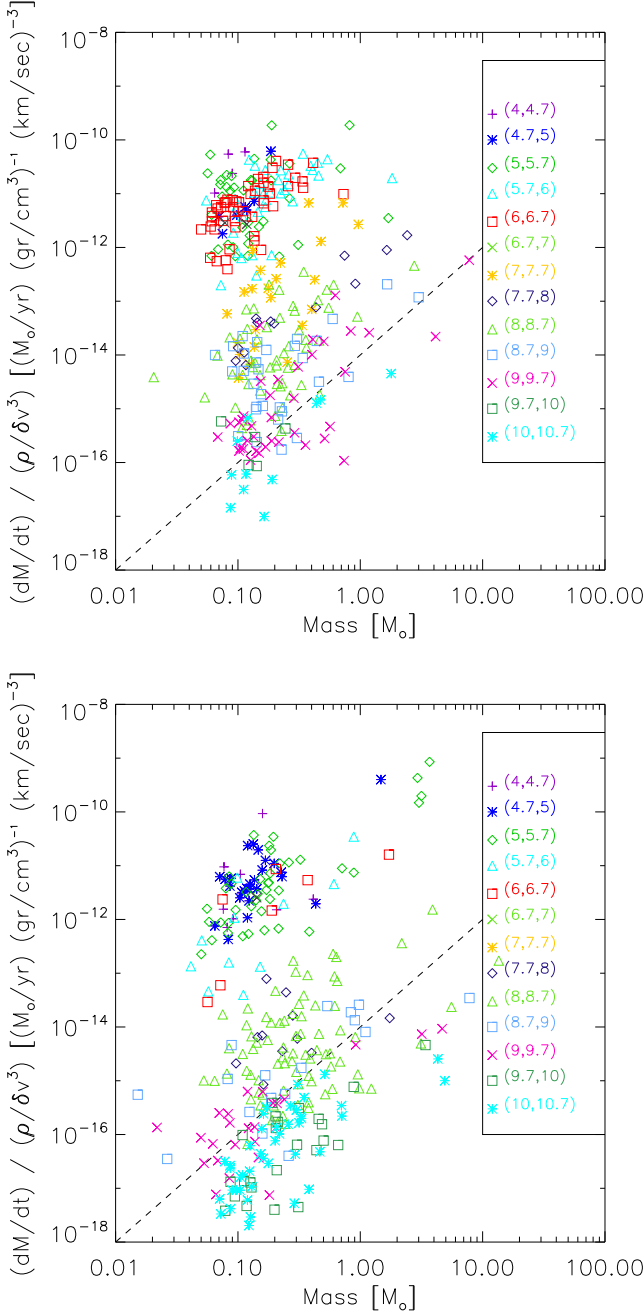


Figure 11. \dot{M}/α' vs. M for runs *a* 22ID2 at $t = 1.03t_{\text{ff}}$ and *b* 32 $t = 1.17t_{\text{ff}}$. The dashed line has a slope of 2, and the actual values of α' are labeled and colored accordingly in the rectangle, in units of $[\text{cm km sec}^{-1}]^{-3}$. Note that when one accounts for the local variations of α' , individual groups exhibit the quadratic dependence of \dot{M} with M .

when we take the ratio \dot{M}/α' , why does the plot \dot{M} vs. M for all the groups exhibits a shallower slope? Should not they all collapse to a single $\dot{M} \propto M^2$ relation, maybe with substantial scatter, when plotting \dot{M} vs. M ? As shown in Fig. 12, where we plot the final mass of each sink vs. the time at which every sink is formed, the most massive sinks systematically form earlier than the lowest-mass sinks, and thus accrete for longer. In other words, *the integration of \dot{M}*

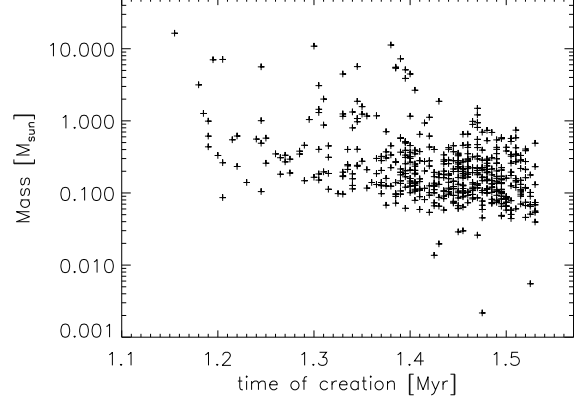


Figure 12. Time at which sinks initially form for Run 32. The sinks with larger final masses systematically accrete for longer than the lowest-mass sinks (see text). Similar plots are found for all the runs.

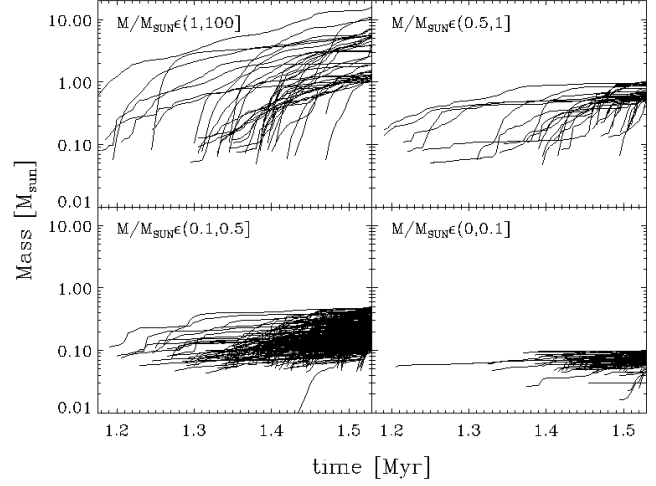


Figure 13. Mass growth vs. time for sinks in run 32, separated into final mass bins for clarity. Upper left, sinks with eventual masses $> 1M_{\odot}$; upper right, sinks with final masses $1.0 < M \leq 0.5M_{\odot}$; lower left, $0.1 < M \leq 0.5M_{\odot}$; lower right, $M \leq 0.1$ sinks.

over time has an implicit dependence on mass. This allows the mass function to evolve to $\Gamma = -1$. Thus, as time proceeds, the *local* environment becomes depleted as it goes into sinks, with the result that earlier-formed sinks accrete somewhat more slowly than when they were created. This environmental depletion is translated in the shallower slopes of individual sink mass evolution vs. time (see Figure 13) than predicted by equation (4) with $\alpha' = \text{cst}^2$. To further support our conclusion, we note that the simulations of Hsu et al. (2010), where all sinks were formed at the same time and continuing sink creation was not allowed, do show $\dot{M} \propto M^2$ for the massive sinks.

The self-gravitating nature of the medium, unlike that

² Note, however, that by imposing a decreasing $\alpha(t)$ as a function of time, one can find individual mass accretion histories similar to those shown in Fig. 13.

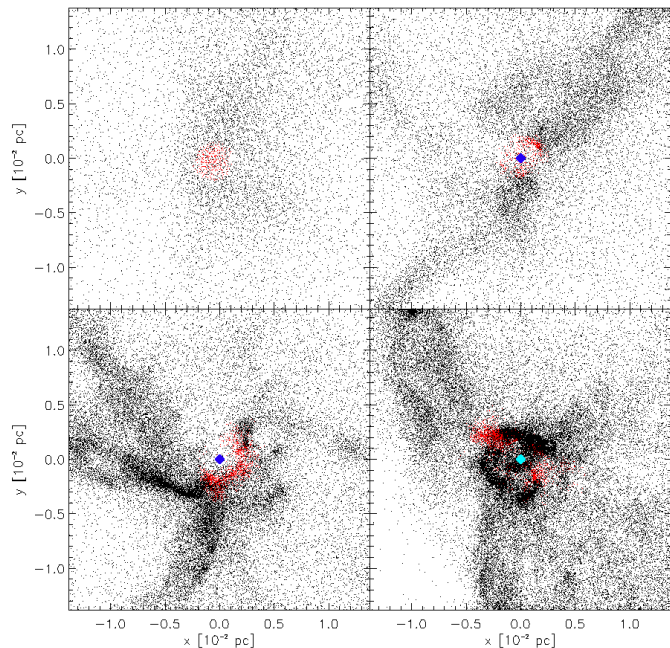


Figure 14. Zoom-in of the time evolution of a region in run 22 which produces one of the earliest, and ultimately most massive, sinks. The sink (when formed) is indicated by the large symbol at (0,0). The red particles are those that will be accreted during the next time step. The “hole” around the sink corresponds to the region $R < R(\text{inner})$, inside of which it is assumed all gas particles accrete. Gravitationally-driven infall via streams is evident (see text).

envisaged in the simple BHL calculation, is responsible for the typically rapid mass growth at early times, as in the “collapse” mode identified by M14. It is not surprising that this is qualitatively different than that predicted by equation (4), as this early evolution represents the initial formation of the gravitating body, and, as such, is not addressed by the BHL formula, which assumes the presence of an already existing mass. One must also recognize that the initial sink mass is only the central condensation of a larger self-gravitating clump. In essence, the early evolution is that of protostellar core collapse; the initial protostellar core has a much lower mass than its surrounding envelope, but the latter is bound by its own self-gravity, not that of the protostellar core. The lack of applicability of gravitational focusing at early stages, however, does not mean that gravitational focusing or quasi-BHL accretion cannot occur later to build the mass well beyond initial collapse values.

One may ask how this differs from models in which turbulence produces an initial clump mass that sets the final mass, even for massive objects (e.g., Padoan & Nordlund 2002; Hennebelle & Chabrier 2008, 2009). We illustrate the difference in Figure 14, where we show the evolution of a region around a sink that forms early and becomes massive. In the upper left panel, the red particles are those that will become part of the initial sink in the next time step (the sink has not yet formed). As described in the previous paragraph, the initial sink mass is only a fraction of the larger self-gravitating clump. As time proceeds, the added mat-

ter arises from gravitationally-driven streams which do not represent initial turbulent fragments.

We note in passing that even though the “velocity fluctuation” models were initiated with a supersonic turbulent velocity field, the motions rapidly decay, leaving density fluctuations as the dominant features which then produce gravitationally-induced supersonic motions. Thus, it may be that initial clump masses are also influenced by gravitational focusing.

4.2 Comparison with other investigations

As noted in the Introduction, in contrast to our findings, M14 concluded that “the upper power law tail of the IMF is unrelated to Bondi-Hoyle accretion”, and, instead, argued that the mass function is the result of a distribution of (initial) seed masses, growth times, and stochastic, fluctuating accretion rates with $\dot{M} \propto M^{-2/3}$. We suggest that the primary reason for the differing conclusions is that their mass function is considerably different from ours. The mass function of M14 (their Figure 11) shows a much broader peak than ours; inspection of their Figure 7 shows that most of the objects in the broad peak of the mass function correspond to “collapse-dominated” sinks, with the mass accreted in only one or two episodes. These objects arguably correspond to “initial” fragmentation masses, and so BHL accretion is undoubtedly irrelevant for these objects (see previous section). However, we also note that the M14 mass function at masses above $1M_{\odot}$ shows an approximate power-law slope of $\Gamma \sim -1.35$. M14 label these “strong” accretors or “accretion-dominated” systems, and we suggest that BHL-type accretion is actually occurring in this mass range.

The broad peak in the M14 mass function relative to ours may reflect, in part, the piecewise barotropic equation of state used by Bonnell et al. (2008), which can affect fragmentation (see discussion in Jappsen et al. (2005)). Our adoption of an isothermal equation of state means that the peaks of our low-mass mass functions are essentially set by our resolution limits rather than by any thermal physics; this likely expands the dynamic range in mass over which BHL accretion can operate, resulting in a clearer development of the Zinnecker power law in our calculations.

As argued in the previous section, the apparent weaker dependence of accretion rate on mass than $\propto M(\text{sink})^2$ does not rule out BHL accretion because of the depletion of environmental gas along with competition between sinks. In fact, when accounting for local variations of α , the quadratic dependence emerges. While M14 obtain an even slower dependence of mass accretion on sink mass than we do, this is partly the result of anchoring the fit at masses below $1M_{\odot}$ (their Figure 6), where accretion beyond the initial fragmentation mass is small.

Finally, M14 also called attention to rapid, large fluctuations in mass accretion rates as a possible problem with BHL accretion; such variations have been seen in other simulations as well (Peters et al. 2010, 2011; Padoan et al. 2014). We also see strong variations in \dot{M} as well, but this variability does not prevent the development of the $\Gamma = -1$ power law. These accretion rate variations reflect clumping in the near-sink environments (see Figure 14). It appears that these clumps are regions which are attempting to fragment and gravitationally collapse, but which fail to do so before being

accreted. In our runs, additional sink formation near existing sinks is prohibited to avoid numerical problems and short time steps as new sinks begin to orbit each other closely. As a test, we reran one of the simulations for a short period of time, removing this constraint, and indeed found additional sinks would form. Thus, it is not clear whether the “ingestion” of this material really represents accretion of gas that will be accreted into the central object, or really represents fragmentation into an additional sink that will simply end up orbiting the first sink. (Of course there is a general issue in this type of simulation, in that resolution limits mean that we are only reporting “system” or “enclosed masses within some radius”.) In our case, the assumption of isothermality probably enhances the tendency toward gravitational clumping. Thus, even though highly variable accretion may be of great interest for understanding the time-variability of protostellar accretion (e.g. Audard et al. 2014), further careful consideration of missing effects such as stellar feedback, magnetic fields, etc. is needed before applying these results to real systems.

5 CONCLUSIONS

Our numerical experiments with simplified physics indicate that gravitational focusing is an effective and plausible means for producing an upper mass power law $\Gamma \sim -1$. The situation is more complicated than in the simplistic analysis of BHL accretion by Zinnecker (1982), but even the temporal and spatial variability, and the presence of nearby gravitating masses, does not prevent the development of the upper mass power law. Although the details of accretion *vs.* time and sink mass are complicated, we argue that the relative accretion rates, integrated over time and space, exhibit an M^2 dependence as in BHL accretion, which produces the power-law mass function we find.

The present set of simulations are obviously quite idealized. Our purpose was to elucidate the basic physics of gravitationally-focused accretion in as easily-visualized and interpretable a situation as possible. While effects of magnetic fields, non-isothermal behavior, and stellar feedback are clearly important to any realistic and comprehensive understanding of the stellar mass function, the results shown here strongly suggest that BHL accretion, understood in its most general sense as an “attractor” with an M^2 dependence on relative accretion rates, remains relevant to an understanding of the upper mass region of the IMF, as previously argued by Bonnell et al. (2001a,b); Clark et al. (2007).

6 ACKNOWLEDGMENTS

We acknowledge an extremely helpful referee report from Ian Bonnell which helped clarify our understanding of the simulation results. This work was supported by UNAM-PAPIIT grant number IN103012 to JBP, and by the University of Michigan, and the Rackham graduate school. Calculations were performed in the supercomputer at DGTIC-UNAM and at the University of Michigan. NPG acknowledges a scholarship from CONACYT. We have made extensive use of the NASA-ADS database.

REFERENCES

- Audard, M., Ábrahám, P., Dunham, M. M., et al. 2014, arXiv:1401.3368
- Bastian, N., Covey, K. R., & Meyer, M. R. 2010, *ARA&A*, 48, 339
- Bate, M. R. 2012, *MNRAS*, 419, 3115
- Bate, M. R., Bonnell, I. A., & Bromm, V. 2003, *MNRAS*, 339, 577
- Bate, M. R., & Burkert, A. 1997, *MNRAS*, 288, 1060
- Bonnell, I. A., Bate, M. R., Clarke, C. J., & Pringle, J. E. 2001, *MNRAS*, 323, 785
- Bonnell, I. A., Clarke, C. J., Bate, M. R., & Pringle, J. E. 2001, *MNRAS*, 324, 573
- Bonnell, I. A., & Bate, M. R. 2006, *MNRAS*, 370, 488
- Bonnell, I. A., Clarke, C. J., & Bate, M. R. 2006, *MNRAS*, 368, 1296
- Bonnell, I. A., Clark, P., & Bate, M. R. 2008, *MNRAS*, 389, 1556
- Clark, P. C., Klessen, R. S., & Bonnell, I. A. 2007, *MNRAS*, 379, 57
- Edgar, R. 2004, *New A Rev.*, 48, 843
- Hennebelle, P., & Chabrier, G. 2008, *ApJ*, 684, 395
- Hennebelle, P., & Chabrier, G. 2009, *ApJ*, 702, 1428
- Hsu, W.-H., Hartmann, L., Heitsch, F., & Gómez, G. C. 2010, *ApJ*, 721, 1531
- Jappsen, A.-K., Klessen, R. S., Larson, R. B., Li, Y., & Mac Low, M.-M. 2005, *A&A*, 435, 611
- Krumholz, M. R., Cunningham, A. J., Klein, R. I., & McKee, C. F. 2010, *ApJ*, 713, 1120
- Maschberger, T., Bonnell, I. A., Clarke, C. J., & Moraux, E. 2014, *MNRAS*, 439, 234
- Myers, A. T., Klein, R. I., Krumholz, M. R., & McKee, C. F. 2014, *MNRAS*, 439, 3420
- Offner, S. S. R., Clark, P. C., Hennebelle, P., et al. 2013, arXiv:1312.5326; also *Protostars and Planets VI*, University of Arizona Press (2014), eds. H. Beuther, R. S. Klessen, C. P. Dullemond, Th. Henning, in press
- Padoan, P., & Nordlund, Å. 2002, *ApJ*, 576, 870
- Padoan, P., Haugbølle, T., & Nordlund, Å. 2014, *ApJ*, 797, 32
- Peters, T., Klessen, R. S., Mac Low, M.-M., & Banerjee, R. 2010, *ApJ*, 725, 134
- Peters, T., Banerjee, R., Klessen, R. S., & Mac Low, M.-M. 2011, *ApJ*, 729, 72
- Springel, V. 2005, *MNRAS*, 364, 1105
- Stone, J. M., Ostriker, E. C., & Gammie, C. F. 1998, *ApJL*, 508, L99
- Zinnecker, H. 1982, *Annals of the New York Academy of Sciences*, 395, 226